

On the inverse Potts functional for single-image super-resolution problems

Pasquale Cascarano, Luca Calatroni, Elena Loli Piccolomini

Abstract—We consider a variational model for single-image super-resolution based on the assumption that the image gradient of the target image is sparse. To promote jump sparsity, we use an isotropic and anisotropic ℓ^0 inverse Potts gradient regularisation term combined with a quadratic data fidelity, similarly as studied in [1] for general problems in signal recovery. For the numerical realisation of the model, we consider a converging ADMM algorithm. Differently from [1], [2], where approximate graph cuts and dynamic programming techniques were used for solving the non-convex substeps in the case of multivariate data, the proposed splitting allows to compute explicitly their solution by means of hard-thresholding and standard conjugate-gradient solvers. We compare quantitatively our results with several convex, non-convex and deep-learning-based approaches for several synthetic and real-world data. Our numerical results show that combining super-resolution with gradient sparsity is particularly helpful for object detection and labelling tasks (such as QR scanning and land-cover classification), for which our results are shown to improve the classification precision of standard clustering algorithms and state-of-the art deep architectures [3].

Index Terms—Single-image super-resolution, inverse Potts functional, jump sparsity, ADMM, QR recognition, land-cover classification.

I. INTRODUCTION

The task of image Super-Resolution (SR) consists in improving the spatial resolution of an observed image by means of a dataset of Low-Resolution (LR) images. Image resolution is limited in many applications due to the optical characteristics and the physical limitations of the system used to acquire it. Some standard examples are image microscopy and astronomic imaging where, due to light aberration phenomena, close objects (molecules, stars...) on LR images cannot be correctly distinguished, see, e.g. [4], [5]. SR techniques are often employed also in image recognition problems. This is the case, for instance, of QR code recognition where images are often captured by scanning tools (e.g. cell-phones) from relatively large distances which may affect the accuracy of the recognition [6]. Analogously, in remote sensing applications such as land-cover classification, only LR measurements are often available, which may limit significantly the classification precision [7], [8].

Among the numerous SR techniques proposed in the literature, we focus in this paper on a Single-image SR model, the

P. Cascarano is with the Department of Mathematics, University of Bologna, 5 Piazza di Porta S. Donato, 40126, Bologna, Italy. Correspondence e-mail: pasquale.cascarano2@unibo.it

L. Calatroni is with CNRS, Université Côte d'Azur, INRIA, I3S, UMR 7271, Sophia-Antipolis, France.

E. Loli Piccolomini is with the Department of Computer Science and Engineering, University of Bologna, 7 Mura Anteo Zamboni, 40126, Bologna, Italy.

easiest SR technique where one single image is employed to compute the desired High-Resolution (HR) output.

Mathematically, it is an ill-posed inverse problem which can be modelled as follows: for a given vectorised LR image $\mathbf{g} \in \mathbb{R}^M$, we look for its HR version $\mathbf{u} \in \mathbb{R}^N$ defined on a space of dimension $N = L^2 M$ with magnification factor $L > 1$ which satisfies the following linear degradation model:

$$\mathbf{g} = \mathbf{S}\mathbf{H}\mathbf{u} + \boldsymbol{\eta}. \quad (1)$$

Here, $\mathbf{S} \in \mathbb{R}^{M \times N}$ stands for the down-sampling operator, $\mathbf{H} \in \mathbb{R}^{N \times N}$ describes blur degradation and $\boldsymbol{\eta}$ is the realisation of an Additive White Gaussian Noise (AWGN) r.v. with zero mean and standard deviation $\sigma_\eta > 0$ in the data.

Due to the ill-posedness of both the operators \mathbf{S} and \mathbf{H} , a standard approach for solving (1) consists in introducing prior knowledge about the solution \mathbf{u} and on the data statistics by means a variational approach. In this framework, an approximated solution $\mathbf{u}^* \in \mathbb{R}^N$ is computed by solving

$$\mathbf{u}^* \in \arg \min_{\mathbf{u} \in \mathbb{R}^N} \frac{1}{2} \|\mathbf{S}\mathbf{H}\mathbf{u} - \mathbf{g}\|_2^2 + \mu R(\mathbf{u}), \quad (2)$$

where the quadratic fidelity term models the presence of Gaussian noise degradation while the regularisation term $R : \mathbb{R}^N \rightarrow \mathbb{R} \cup \{+\infty\}$ encodes prior information on the target image \mathbf{u} , thus ensuring the stability of the inversion process. The two terms are balanced by a regularisation parameter $\mu > 0$. We refer the reader to [9], [10] and to the references therein for a review on variational approaches for SR problems.

A. Related works

Classical variational approaches to the SR problem are based on the use of least squares, Fourier series and Tikhonov-type gradient regularisations [9], which favour noise removal at the price of creating smoothing and ringing artefacts which are undesirable in many applications such as object detection, where images with sharper edges are preferable for better classification. To overcome this drawback, the use of edge-preserving convex regularisation terms based on the idea of gradient sparsity, such as Total Variation (TV) regularisation in [11], [12] along with its fractional variations in [13], has been proposed. Such methods have shown good performances in many applications, although in many situations they still suffer from either reconstruction artefacts (e.g. staircasing, loss of contrast...) and/or numerical inefficiency which limits their practical use in segmentation/classification problems.

In recent years, sparse and non-convex regularisation approaches have become very popular in the context of image

reconstruction due to their better ability of preserving sharp edges even in low-contrast scenarios. A significant contribution in this direction has been made by Storath et al. in a series of papers [1], [2], [14] where the use of the ℓ^0 pseudo-norm on the image gradient magnitude (see [15]) has been thoroughly studied for several imaging problems (deconvolution, sparse recovery, joint reconstruction and segmentation...). The gradient smoothing favoured by the *inverse Potts model* studied in these works has been shown to be in fact very useful in many situations where a further classification/labelling step is required. It is natural to study how this model performs on SR problem where the presence of a further down-sampling operator \mathbf{S} in (1) makes the problem more challenging.

Different approaches for solving the SR problem make use of deep architectures to encode prior information on the desired HR solution by means of a training set of examples [16]–[18]. In particular, in [19] the authors present a Plug-and-Play (PnP) framework, later developed in [20], [21], which exploits Deep convolutional neural network denoisers embedded in standard optimisation algorithms, such as Alternating Direction of Multipliers (ADMM) or Half-Quadratic Splitting (HQS), which induce prior information on the desired HR solution. Differently from model-based variational approaches, deep learning-based methods do not require an explicit expression of the regularisation term R , since this can be learned directly from the data and adapted to the particular application considered. Those methods have currently reached state-of-the-art performances in several image reconstruction problems, although their theoretical foundation and their stability to perturbation in the data is still debated.

B. Contribution

We consider a variational model for solving the single-image SR problem (1) where a ℓ^0 jump-sparsity regularisation is combined with a quadratic data fidelity term. In order to adapt the regularisation to possible orthogonal geometric structures (as it is desirable, for instance, in the case of QR recognition tasks), we propose both a coupled (isotropic) and decoupled (anisotropic) regularisation. From a numerical point of view, we propose a novel convergent ADMM algorithm decomposing the original problem into substeps which can be solved efficiently by means either of a direct hard-thresholding or by means of standard linear solvers. Note that the proposed splitting differs from the one introduced by Storath et al. [1], [2], [14], where the non-smooth substeps need to be solved either by means of approximate graph-cuts approaches [22] or by a sequence of dynamic programming algorithms. We test our model on real-world applications where an accurate HR version of the given LR image \mathbf{g} is required in view of further detection or classification tasks (QR scanning, land-cover labelling), showing that the proposed model improves significantly the labelling precision for different classification modalities. Up to our knowledge, the use of the inverse Potts functional on real-world SR problems and its comparisons with state-of-the art convex, non-convex and deep-learning-based approaches is something that has not been sufficiently covered in the existing literature.

C. Organisation of the paper

In Section II we provide a quick review of jump-sparse variational methods for single-image SR. In Section III we present a novel converging ADMM scheme for solving the proposed model along with a detailed description of its practical realisation. In Section IV we report some numerical tests on the sensitivity of the model to its parameters on synthetic images. Finally, in Section V we apply our model to some real-world applications such as QR scanning, JPG artefact reduction and land-cover classification. We report the convergence proofs in Appendix A to improve the flow of the manuscript.

II. JUMP-SPARSE IMAGE SUPER-RESOLUTION MODELS

The use of convex edge-preserving regularisation for single- and multi-image SR problems has been proposed first in [11], [12]. In these works, by denoting the discretised image gradient of $\mathbf{u} \in \mathbb{R}^N$ endowed with suitable boundary conditions by $\mathbf{Du} = (\mathbf{D}_h \mathbf{u}, \mathbf{D}_v \mathbf{u}) \in \mathbb{R}^{2 \times N}$, the proposed TV term reads:

$$R(\mathbf{u}) = \|\mathbf{Du}\|_{1,p} = \sum_{i=1}^N (|(\mathbf{D}_h \mathbf{u})_i|^p + |(\mathbf{D}_v \mathbf{u})_i|^p)^{1/p}, \quad (3)$$

where $p \in \{1, 2\}$ favours anisotropic or isotropic regularisation. Fractional generalisations to exponents $1 < p < 2$ are also possible [13].

A. The isotropic and anisotropic inverse Potts functional

Jump-sparsity can be enforced also by means of non-convex ℓ^0 gradient smoothing, see, e.g., [15] and [1]. In such case and similarly as above, for $p \in \{1, 2\}$ we can thus consider the following regularisation functional:

$$\begin{aligned} R(\mathbf{u}) &= \|\mathbf{Du}\|_{0,p} & (4) \\ &:= \sum_{i=1}^N \begin{cases} \|\mathbf{D}_h \mathbf{u}\|_2 \mid_0 + \|\mathbf{D}_v \mathbf{u}\|_2 \mid_0 & \text{for } p = 1, \\ \|\mathbf{D}_h \mathbf{u}, \mathbf{D}_v \mathbf{u}\|_2 \mid_0 & \text{for } p = 2, \end{cases} \end{aligned}$$

where by $|\cdot|_0$ we denote the function:

$$|z|_0 := \begin{cases} 0 & z = 0 \\ 1 & z \neq 0. \end{cases}$$

For a generic vector $\mathbf{z} \in \mathbb{R}^n$, $\|\mathbf{z}\|_0 := \sum_i |z_i|_0$ is often called the ℓ^0 pseudo-norm of \mathbf{z} . Thus, by definition, the functional (4) counts the number of jumps of \mathbf{u} by means of the gradient magnitude map. In particular, in the case $p = 1$ the regulariser counts the jumps along the two orthogonal horizontal/vertical gradient directions independently, while for $p = 2$ magnitudes are taken into account jointly. In both cases, the term $\|\mathbf{Du}\|_{0,p}$ penalises low-amplitude structures while preserving sharp edges in images, thus favouring piece-wise constant reconstructions which are particularly desirable for further multi-class segmentation problems. We further notice that $0 \leq \|\mathbf{Du}\|_{0,p} \leq 2N$ for $p \in \{1, 2\}$.

In the following, we will refer to (4) with $p = 1$ as the *anisotropic* jump-sparsity (TV0A) regularisation, in contrast to the case $p = 2$ which we will refer to as the *isotropic* regularisation (TV0I), in analogy with the terminology used for TV in (3).

III. A NOVEL ADMM SPLITTING ALGORITHM

For $p \in \{1, 2\}$, we consider the SR problem (2) with the choice (4), that is:

$$\mathbf{u}^* \in \arg \min_{\mathbf{u} \in \mathbb{R}^N} \left\{ \Phi(\mathbf{u}; \mu, p) := \frac{1}{2} \|\mathbf{SHu} - \mathbf{g}\|_2^2 + \mu \|\mathbf{Du}\|_{0,p} \right\}. \quad (5)$$

This problem is non-convex and non-smooth. The existence of minimisers is guaranteed by the following theorem whose proof can be easily adapted following [1, Theorem 1].

Theorem 1: The solution sets of both the anisotropic ($p = 1$) and the isotropic ($p = 2$) inverse Potts SR problems (5) are non-empty.

To solve numerically problem (5) we propose in the following an iterative *alternating method of multipliers* (ADMM) which has been extensively used in the context of TV minimisation problems e.g. in [23], [24] and also adapted to ℓ^0 gradient-sparse problems in [1], [2]. We divide the description for the anisotropic and isotropic case.

A. ADMM for the anisotropic inverse Potts problem

For $p = 1$, we can rewrite the unconstrained minimization problem (5) in the following equivalent constrained form:

$$\begin{aligned} \arg \min_{\mathbf{u}} \frac{1}{2} \|\mathbf{SHu} - \mathbf{g}\|_2^2 + \mu (\|\mathbf{t}\|_0 + \|\mathbf{s}\|_0) \\ \text{s.t.} \quad \mathbf{t} := \mathbf{D}_h \mathbf{u}, \quad \mathbf{s} := \mathbf{D}_v \mathbf{u} \end{aligned}$$

where $\mathbf{t}, \mathbf{s} \in \mathbb{R}^N$ are the horizontal/vertical gradient components, respectively.

We can then define the augmented Lagrangian function:

$$\begin{aligned} L_{\beta_t, \beta_s}(\mathbf{u}; \mathbf{t}, \mathbf{s}, \boldsymbol{\lambda}_t, \boldsymbol{\lambda}_s) := \frac{1}{2} \|\mathbf{SHu} - \mathbf{g}\|_2^2 + \mu \|\mathbf{t}\|_0 + \mu \|\mathbf{s}\|_0 \\ + \langle \boldsymbol{\lambda}_t, \mathbf{D}_h \mathbf{u} - \mathbf{t} \rangle + \frac{\beta_t}{2} \|\mathbf{D}_h \mathbf{u} - \mathbf{t}\|_2^2 + \langle \boldsymbol{\lambda}_s, \mathbf{D}_v \mathbf{u} - \mathbf{s} \rangle \\ + \frac{\beta_s}{2} \|\mathbf{D}_v \mathbf{u} - \mathbf{s}\|_2^2 \end{aligned} \quad (6)$$

where β_t and β_s are two positive penalty parameters and $\boldsymbol{\lambda}_t$ and $\boldsymbol{\lambda}_s$ are the vectors of Lagrange multipliers related to the auxiliary variables \mathbf{t} and \mathbf{s} , respectively. By letting the two parameters β_t, β_s increase along the iterations (we will provide specific growth condition in the following Theorem 2), we can then minimise (6) with respect to \mathbf{t}, \mathbf{s} and \mathbf{u} by iterating the following scheme:

$$\left\{ \begin{aligned} \mathbf{t}^{k+1} &\in \arg \min_{\mathbf{t}} \mu \|\mathbf{t}\|_0 + \frac{\beta_t^k}{2} \|\mathbf{t} - (\mathbf{D}_h \mathbf{u}^k + \frac{\boldsymbol{\lambda}_t^k}{\beta_t^k})\|_2^2 \end{aligned} \right. \quad (7)$$

$$\left. \begin{aligned} \mathbf{s}^{k+1} &\in \arg \min_{\mathbf{s}} \mu \|\mathbf{s}\|_0 + \frac{\beta_s^k}{2} \|\mathbf{s} - (\mathbf{D}_v \mathbf{u}^k + \frac{\boldsymbol{\lambda}_s^k}{\beta_s^k})\|_2^2 \end{aligned} \right. \quad (8)$$

$$\left\{ \begin{aligned} \mathbf{u}^{k+1} &= \arg \min_{\mathbf{u}} \frac{1}{2} \|\mathbf{SHu} - \mathbf{g}\|_2^2 + \\ &+ \frac{\beta_t^k}{2} \|\mathbf{D}_h \mathbf{u} - (\mathbf{t}^{k+1} - \frac{\boldsymbol{\lambda}_t^k}{\beta_t^k})\|_2^2 + \frac{\beta_s^k}{2} \|\mathbf{D}_v \mathbf{u} - (\mathbf{s}^{k+1} - \frac{\boldsymbol{\lambda}_s^k}{\beta_s^k})\|_2^2 \end{aligned} \right. \quad (9)$$

$$\boldsymbol{\lambda}_t^{k+1} = \boldsymbol{\lambda}_t^k - \beta_t^k (\mathbf{t}^{k+1} - \mathbf{D}_h \mathbf{u}^{k+1}) \quad (10)$$

$$\boldsymbol{\lambda}_s^{k+1} = \boldsymbol{\lambda}_s^k - \beta_s^k (\mathbf{s}^{k+1} - \mathbf{D}_v \mathbf{u}^{k+1}), \quad (11)$$

where a gradient ascent update of the Lagrange multipliers is also applied. We have the following convergence result (the proof is given in Appendix A).

Theorem 2: Let (β_t^k) and (β_s^k) be the increasing sequences of penalty parameters in the ADMM scheme (7)-(11). If $\frac{k}{\beta_t^k} \rightarrow 0$, $\frac{k}{\beta_s^k} \rightarrow 0$ and $\frac{\beta_s^k}{\beta_t^k} \rightarrow c$ with $c \in \mathbb{R}^*$ and the operators \mathbf{D}_h and \mathbf{D}_v are full rank, then the ADMM iterations (7), (8), (9) converge to \mathbf{t}^* , \mathbf{s}^* and \mathbf{u}^* respectively and there holds $\mathbf{D}_h \mathbf{u}^* = \mathbf{t}^*$ and $\mathbf{D}_v \mathbf{u}^* = \mathbf{s}^*$.

We remark that the full rank assumption on the operators \mathbf{D}_h and \mathbf{D}_v is verified, for instance, if Dirichlet boundary conditions are assumed. A sufficient condition which guarantees the required growth of the penalty parameter is that $\beta_t^k = \beta_s^k = O(k^{1+\epsilon})$, $\epsilon > 0$.

B. ADMM for the isotropic inverse Potts problem

For $p = 2$ we can similarly re-write the problem (5) in the following equivalent constrained form:

$$\begin{aligned} \arg \min_u \frac{1}{2} \|\mathbf{SHu} - \mathbf{g}\|_2^2 + \mu \sum_{i=1}^N \|\mathbf{z}_i\|_2 \quad (12) \\ \text{s.t.} \quad \mathbf{z} := \mathbf{Du} \end{aligned}$$

where $\mathbf{z}_i := ((\mathbf{D}_h \mathbf{u})_i, (\mathbf{D}_v \mathbf{u})_i) \in \mathbb{R}^2$, for each $i = 1, \dots, N$. The augmented Lagrangian function reads in this case:

$$\begin{aligned} L_\beta(\mathbf{u}; \mathbf{z}, \boldsymbol{\lambda}_z) := & \frac{1}{2} \|\mathbf{SHu} - \mathbf{g}\|_2^2 + \mu \sum_{i=1}^N \|\mathbf{z}_i\|_2 \\ & + \langle \boldsymbol{\lambda}_z, \mathbf{Du} - \mathbf{z} \rangle + \frac{\beta}{2} \|\mathbf{Du} - \mathbf{z}\|_2^2 \end{aligned} \quad (13)$$

where $\beta > 0$ is a scalar penalty parameter and $\boldsymbol{\lambda} \in \mathbb{R}^{2 \times N}$ is the Lagrange multiplier. As above, by letting the penalty parameter increase along the iterations (see the following Theorem 3), we seek for minimisers of (13) by iterating the following scheme:

$$\left\{ \begin{aligned} \mathbf{z}^{k+1} &\in \arg \min_{\mathbf{z}} \mu \sum_{i=1}^N \|\mathbf{z}_i\|_2 + \frac{\beta^k}{2} \|\mathbf{z} - (\mathbf{Du}^k + \frac{\boldsymbol{\lambda}^k}{\beta^k})\|_2^2 \end{aligned} \right. \quad (14)$$

$$\left. \begin{aligned} \mathbf{u}^{k+1} &= \arg \min_{\mathbf{u}} \frac{1}{2} \|\mathbf{SHu} - \mathbf{g}\|_2^2 + \frac{\beta^k}{2} \|\mathbf{Du} - (\mathbf{z}^{k+1} - \frac{\boldsymbol{\lambda}^k}{\beta^k})\|_2^2 \end{aligned} \right. \quad (15)$$

$$\boldsymbol{\lambda}^{k+1} = \boldsymbol{\lambda}^k - \beta^k (\mathbf{z}^{k+1} - \mathbf{Du}^{k+1}) \quad (16)$$

Similarly as above, we have the following convergence result (see Appendix A for the proof):

Theorem 3: Let (β^k) the increasing sequences of penalty parameters in the ADMM scheme (14)-(16). If $\frac{k}{\beta^k} \rightarrow 0$, and the operator \mathbf{D} is full rank, then the ADMM iterations (14), (15) converge to \mathbf{z}^* and \mathbf{u}^* respectively and there holds $\mathbf{Du}^* = \mathbf{z}^*$.

C. Solution of ADMM subproblems

We report here some practical details on how we solve the ADMM schemes (7)-(9) and (14)-(15).

Solution of ℓ^0 subproblems: Due to decomposability of the ℓ^0 term, solving problems (7), (8) corresponds to solve N one-dimensional ℓ^0 problems in the form:

$$\arg \min_{\mathbf{t}_i \in \mathbb{R}} \delta |\mathbf{t}_i|_0 + (\mathbf{t}_i - \mathbf{f}_i)_2^2$$

where $\delta = \frac{2\mu}{\beta_t^k}$ and $\mathbf{f} = \mathbf{D}_h \mathbf{u}^k + \frac{\lambda_t^k}{\beta_t^k}$ for (7), while $\delta = \frac{2\mu}{\beta_s^k}$, $\mathbf{f} = \mathbf{D}_v \mathbf{u}^k + \frac{\lambda_s^k}{\beta_s^k}$ for (8). Solving these problems correspond to compute the proximal map of $|\cdot|_0$ evaluated in \mathbf{f}_i , which is nothing but the hard-thresholding [25]. As far as the problem (14) is concerned, it can be similarly be reduced to the solution of N two-dimensional ℓ^0 -regularised problems in the form:

$$\arg \min_{\mathbf{z}_i \in \mathbb{R}^2} \delta \|\mathbf{z}_i\|_2 |_0 + \|\mathbf{z}_i - \mathbf{f}_i\|_2^2 \quad (17)$$

where $\delta = \frac{2\mu}{\beta^k}$ and $\mathbf{f}_i = (\mathbf{D}_h \mathbf{u}_i^k + \frac{\lambda_t^k}{\beta^k}, \mathbf{D}_v \mathbf{u}_i^k + \frac{\lambda_s^k}{\beta^k})$. Each 2D minimization problem in (17) can be solved by computing the 2D proximal map of ℓ^0 evaluated in \mathbf{f}_i following [15].

Solution of the quadratic subproblems: Let us define $\mathbf{K} := \mathbf{S}\mathbf{H}$. Problems (9) and (15) are two standard quadratic minimisation problems, thus their minimisers are given by the solution of their normal equations, which read respectively:

$$\begin{aligned} (\mathbf{K}^T \mathbf{K} + \beta_t^k \mathbf{D}_h^T \mathbf{D}_h + \beta_s^k \mathbf{D}_v^T \mathbf{D}_v) \mathbf{u} &= \\ &= \mathbf{K}^T \mathbf{g} + \beta_t^k \mathbf{D}_h^T \mathbf{f}_t + \beta_s^k \mathbf{D}_v^T \mathbf{f}_s, \end{aligned}$$

$$(\mathbf{K}^T \mathbf{K} + \beta^k \mathbf{D}^T \mathbf{D}) \mathbf{u} = \mathbf{K}^T \mathbf{g} + \beta^k \mathbf{D}^T \mathbf{f},$$

where $\mathbf{f}_t = \mathbf{t}^{k+1} - \frac{\lambda_t^k}{\beta_t^k}$, $\mathbf{f}_s = \mathbf{s}^{k+1} - \frac{\lambda_s^k}{\beta_s^k}$ and $\mathbf{f} = \mathbf{z}^{k+1} - \frac{\lambda^k}{\beta^k}$. The dimension of the previous linear systems is typically very large. For solving them efficiently, we thus make use of Conjugate Gradient (CG) algorithm, which we speed-up using a warm-start initialisation at every iteration.

Note that the computational complexity for solving the ℓ^0 subproblems is $O(N)$, while the cost for solving (9) and (15) is $O(N^2)$ for each CG iteration.

D. Comparisons with previous splittings

The variable splitting (and, therefore, the ADMM scheme) we consider here is different than the one considered in [1], [2], [14] which corresponds to set $\mathbf{z} = \mathbf{u}$ in (12). Our choice avoids the presence of the gradient in the ℓ^0 minimization problems (7)-(8) and (14), leading to a faster computation of the solution of these problems without requiring the use of approximate solvers as it was done in [1] where the authors use approximate graph-cut algorithms for solving these subproblems. These algorithms have well-known drawbacks such as strong dependence on the initialisation and the need of an inner iterative approximate solver [2], [26]. As an alternative, in [2], the isotropic substep is solved by a set of anisotropic problems along the diagonal or knight-move directions, which are solved by dynamic programming approaches with overall computational of $O(N^2)$. In order to guarantee the convergence of the sequence (\mathbf{u}_k) to the limiting point \mathbf{u}^* (see Appendix A), it turns out to be fundamental the full rank assumption of the operators \mathbf{D}_h and \mathbf{D}_v . We stress, however, that this is not very limiting since Dirichlet boundary conditions can always be imposed by an artificial image padding of the image. In our numerical experiments, however, we observe numerical convergence even if periodic boundary conditions are used for the discretisation of the gradient $\mathbf{D}\mathbf{u}$. A theoretical convergence proof in this case is left for future research. As far as the growth condition

on the penalty parameters is concerned, we remark that in [1] a geometric growth was assumed. Unfortunately, this is not enough for our theoretical convergence result to hold, as oscillations may appear if this is violated. We illustrate with some numerical examples the importance of this growth condition in Section V-A.

IV. IMPLEMENTATION NOTES

We report in this section some details regarding the practical implementation of the models discussed above.

1) Operators: For the following synthetic examples we simulate the LR given image starting from a ground-truth HR image and applying the model (1). In particular, we set \mathbf{S} as the discretised 2D Lanczos down-sampling operator [27], using the inbuilt MATLAB function `imresize`. The blur matrix \mathbf{H} is computed by assuming a Gaussian PSF with zero mean and standard deviation σ_H which will be specified later on. Finally, we consider AWGN with zero mean and standard deviation σ_η whose values will be made precise in the following.

2) Comparisons: We compare the results obtained by means of our approach with other models based on jump-sparse regularisation such as convex TV [12] and non-convex capped- L_1 (cL1) regularisations [28], which, for consistency, we have implemented within the same ADMM optimisation framework. We further compare our results with the ones obtained by two state-of-the-art Deep Learning-based approaches. The former is the Enhanced Deep Super-Resolution (EDSR) [18] approach, a Convolutional Neural Network winner of the NTIRE Challenge 2017 [29]. For that, we use a model trained on the dataset DIV2K¹, which consists of 16 residual blocks, 64 filters and 1.5 million weights. The latter is the Image Restoration Convolutional Neural Network (IRCNN) [21], which is a PnP method based on Half Quadratic Splitting (HQS) optimisation.

3) Initialization, parameters and evaluation metrics: We initialise the starting image \mathbf{u}_0 as the Lanczos up-scaling applied to the low resolution image \mathbf{g} . Since the problem (5) is highly non-convex, we actually tested different starting points (the aforementioned one, the zero image and the TV initialisation) and kept the one providing the best results. However, it is worth remarking that we did not observe dramatic changes in the results for these different initialisations. We then initialise the auxiliary variables $\mathbf{t}, \mathbf{s}, \mathbf{v}$ as well as the dual variables $\lambda_t, \lambda_s, \lambda_v$ in (7)-(11) and in (14)-(16) to 0. To ensure the algorithmic convergence stated by the Theorems 2 and 3, the penalty sequences are fixed as $(\beta_k) = k^{1+\epsilon}$ with $\epsilon = 10^{-4}$. The process is stopped when the relative change between consecutive iterates \mathbf{u}^k is lower than 10^{-4} .

For simulated data, we evaluate the quality of the SR images obtained by means of the widely used Peak-Signal-to-Noise-Ratio (PSNR) and Mean Structure Similarity (SSIM) [30] indices as well as the Jaccard index, frequently employed for the evaluation of localisation algorithms in the context of microscopy imaging, see, e.g., [31] for a review.

¹<https://github.com/krasserm/super-resolution>

V. EXPERIMENTS

We report here several experiments on synthetic and real problems. All the experiments are executed on a PC Intel(R) Core(TM) i5-6200U CPU @ 2.30 GHz 2.40GHz with 8.00Gb RAM using Matlab R2018b and Python 3.

We first analyse the performance of the algorithm and its sensitivity to the choice of its parameters on some synthetic examples. Next, we apply our model to three different SR real-world applications: LR QR code reconstruction, JPG artefacts removal and land-cover classification from hyperspectral images. The codes are available at <https://github.com/pcascarano>.

A. Computational analysis on synthetic data

We start considering a synthetic test problem and visualize the reconstructions obtained for different choices of the regularisation parameter μ .

We generate LR data by applying the model (1) starting from the HR 428×600 pixels grayscale image of a butterfly (Figure 1 (a)). We blur the image by using a Gaussian blur with $\sigma_H = 1$, down-sample it by a factor $L = 4$ and add AGWN with standard deviation $\sigma_\eta = 0.01$ (see Figure 1 (b)). In Figure 1 (c)-(f) we report the results computed by the anisotropic and isotropic inverse Potts model for two different values of the regularisation parameter $\mu \in \{0.005, 0.01\}$. The jump-sparse regularisation flattens out many details in the reconstruction, promoting a cartoon-like reconstruction which can be easily used for subsequent classification and segmentation purposes: the higher the regularisation parameter μ , the more simplified the reconstruction. We further add two close-ups of two ROIs (labelled by blue and red frames): the blue square contains both fine details (filaments, yellow arrows) and corner points (green arrows), the red one textured details. The directional bias of the TV0A regularisation along the horizontal and vertical direction is here clearly visible. We report in the captions of the Figure 1 (c)-(f) the values of TV0A and of TV0I computed in correspondence of the result \mathbf{u}^* , which corresponds to the number of gradient jumps on the final image. Choosing a larger μ , more jump-sparsity is promoted so the number of jumps on the final image is smaller.

We now study how the algorithmic convergence depends on the choice of the penalty sequences. We thus report in Figure 2 (a) and 2 (b) the convergence plots for the anisotropic and isotropic inverse Potts model, respectively. In particular, on the left part of the plot we show the behaviour of the objective functions $\Phi(\mathbf{u}^k; \mu, p)$ along the ADMM iterations for different choices of the penalty sequences. For both cases $p = 1$ and $p = 2$ we choose $\beta^k = \beta_t^k = \beta_s^k \equiv 10$ for all k (blue line), $\beta^k = \beta_t^k = \beta_s^k = k^{0.5}$ (red line) and $\beta^k = \beta_t^k = \beta_s^k = k^{1+\epsilon}$ with $\epsilon = 10^{-4}$ (yellow line). On the right part of the plots we further show the decay of the quadratic data term. We observe that if the penalty sequence fulfills the required polynomial growth then the convergence is nicely monotone. while for the other two choices which violate the required polynomial growth, the cost may exhibit nonetheless oscillations. Numerically, this suggests that possibly less severe growth conditions (in particular, sufficiently large constant values of the penalty

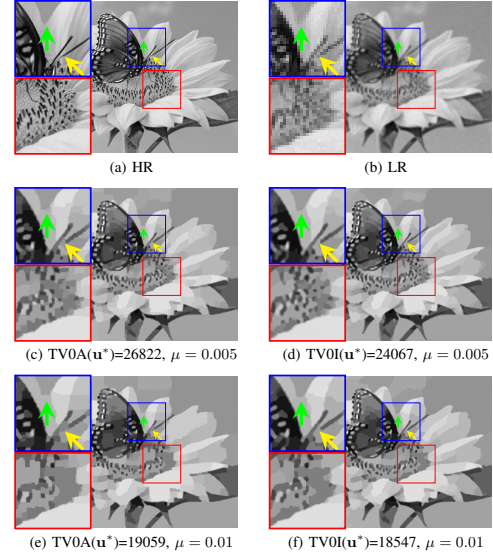


Figure 1: Results obtained for different regularisation parameters μ by the anisotropic and isotropic inverse Potts model for SR on a synthetic image.

parameters) may be employed. A further study on this is left for future research.

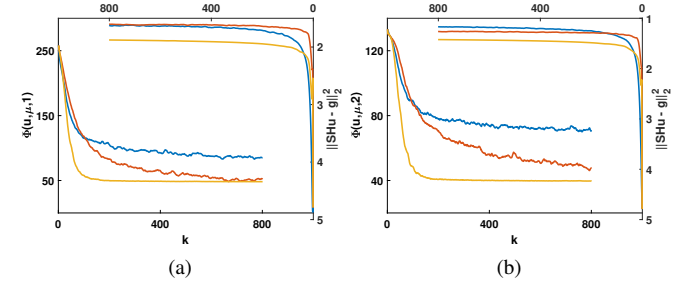


Figure 2: Values of the cost function (left y -axis) and of the fidelity term (right y -axis) along iterations (bottom and top horizontal axis) for different choices of the penalty parameter sequences in the two cases $\Phi(\mathbf{u}^k; \mu, 1)$ (a) and $\Phi(\mathbf{u}^k; \mu, 2)$ (b). The coloured lines correspond to the choices $\beta^k = \beta_t^k = \beta_s^k \equiv 10$ (blue), $\beta^k = \beta_t^k = \beta_s^k = k^{0.5}$ (red), $\beta^k = \beta_t^k = \beta_s^k = k^{1+\epsilon}$ with $\epsilon = 10^{-4}$ (yellow).

B. Real-world applications

In this section we report the results obtained by applying the proposed model to three different real-world applications where a joint magnification and simplification of the given image is desired.

1) *QR code recognition*: The first application we consider is the problem of QR super-resolution. As described in, e.g., [6], images of QR codes are often scanned nowadays by means of portable devices with limited resolution. Furthermore, QR scans are often taken from a distance and in non-optimal optical conditions so that blur and noise further limit the amount of visible information, thus making the use of SR models desirable.

To test our model, we first generate a binary QR code image of size 250×250 by using a free QR code generator ², then

²<https://www.qrme.co.uk/>

we simulate several LR acquisitions for different levels of degradation. We consider three test cases: $\sigma_\eta = 0.01$ and $\sigma_H = 1$ (TEST 1), $\sigma_\eta = 0.05$ and $\sigma_H = 1$ (TEST 2) and $\sigma_\eta = 0.01$ and $\sigma_H = 4$ (TEST 3).

We compare the results by our model with the ones obtained by the models mentioned in Section IV-2. For each method, we select the best model parameters maximising the Jaccard index. Furthermore, to avoid non-binary output pixels, we post-process the SR results by means of an adaptive Otsu binarisation and re-compute the evaluation metrics on the binary output, see Table I.

In Figure 3 we report the results obtained by the different methods for the TEST 2 image before (red frame) and after (blue frame) binarisation. We observe that due to the nature of the the TV0-type regularisations, these results are almost binary so they do not benefit from the post-processing step, while the other methods do. In Figure 4 we report a zoom of the best results obtained before binarisation by the methods starting from a highly corrupted LR image (TEST3).

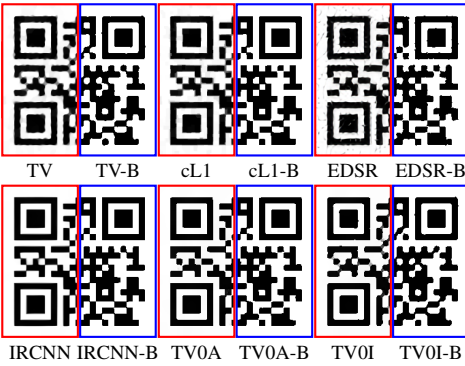


Figure 3: QR SR by using different SR methods (TEST2). In the red left frame we report the output obtained by the different methods considered, in the blue frame their binarisation.

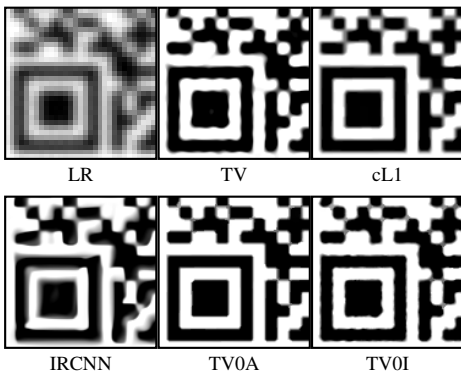


Figure 4: Details of QR SR outputs by using different SR methods (TEST 3).

The quantitative evaluation of the results for the three different test cases is reported in Table I where we show several quality indices for all the methods considered. Without any binarisation, the TV0A model outperforms all the others as far as the PSNR, SSIM and Jaccard indices are concerned. The simplified geometry of the QR images considered (and

the sole presence of horizontal/vertical edges) makes in fact this kind of data suitable for strongly-biased regularisation. Furthermore, the highly non-convex jump-sparsification forces the ouput to be almost binary, without the need of any further post-processing binarisation, as it is required by all the other regularisations to achieve comparable (if not better) quality scores. This simple example shows that the image simplification intrinsically favoured by the use of TV0 regularisers may avoid further post-processing. We point out here that choosing the right evaluation metric for this kind of problems is not trivial. While PSNR and SSIM can quantify more model performance in terms of reconstruction quality, the Jaccard index is more appropriate to assess correct versus false pixel localisation.

As far as the deep-learning results are concerned, we remark that the EDSR neural network in this experiment is used in a transfer learning mode, with no noisy nor blurred images observed in the training phase. For a fairer comparison, we thus consider the IRCNN PnP approach which is capable to handle different level of degradations.

Table I: Quantitative evaluation of QR SR models for different degradation levels. For all methods, the model parameters have been selected maximising the Jaccard Index. By “-B” we denote the results obtained after adaptive Otsu image binarisation. In each column we colour red the best method, and blue the second-best method.

LR	Method	PSNR	PSNR-B	SSIM	SSIM-B	Jaccard
TEST 1	TV0I	22.5199	29.0809	0.9423	0.9873	0.9980
	TV0A	32.5943	35.8478	0.9913	0.9989	0.9998
	TVI	23.3845	26.3357	0.9489	0.9762	0.9963
	cL1	19.4522	36.7496	0.8849	0.9977	0.9997
	EDSR	20.4428	27.4751	0.8210	0.9843	0.9971
	Zhang	25.0589	35.3363	0.9622	0.9992	0.9995
TEST 2	TV0I	19.3318	18.6308	0.8766	0.9156	0.9781
	TV0A	22.6887	22.6256	0.9242	0.9653	0.9912
	TVI	18.1101	18.9848	0.8012	0.9171	0.9798
	cL1	18.7331	21.3473	0.8211	0.9595	0.9882
	EDSR	18.2167	19.1326	0.6810	0.9109	0.9805
	Zhang	21.4314	26.3968	0.9057	0.9850	0.9902
TEST 3	TV0I	18.3763	19.7532	0.8634	0.9294	0.9831
	TV0A	19.2908	21.9341	0.8861	0.9556	0.9897
	TVI	17.9552	20.1585	0.8222	0.9282	0.9846
	cL1	16.9580	22.4648	0.7915	0.9605	0.9917
	EDSR	11.1517	11.1496	0.3993	0.6041	0.8781
	Zhang	14.2915	12.5640	0.6342	0.6565	0.9133

2) *JPG artefacts removal*: In [1], [15], [32] the problem of JPG artefact removal has been deeply addressed by means of jump-sparse regularisation. Here, we consider a more complex scenario where artefact removal is performed together with a resolution improvement. To do so, we consider a LR cartoon-type image of size $170 \times 170 \times 3$ suffering from JPG compression artefacts and with small, not discernible details, and apply the anisotropic/isotropic inverse Potts model and their competitors. For each model, we empirically select the parameters producing the best visual output: since the ground-truth image is not available in this case, we can in fact comment on the results only in terms of visual quality.

In Figure 5 we report two close-ups of the computed SR reconstructions marked with blue and red boxes. The blue box highlights small details which are not discernible in the LR image, while the red box considers a patch of the face with some blunt edges and a small (but important!) face mole. We see that both TV0A and TV0I reconstructions are sharper and

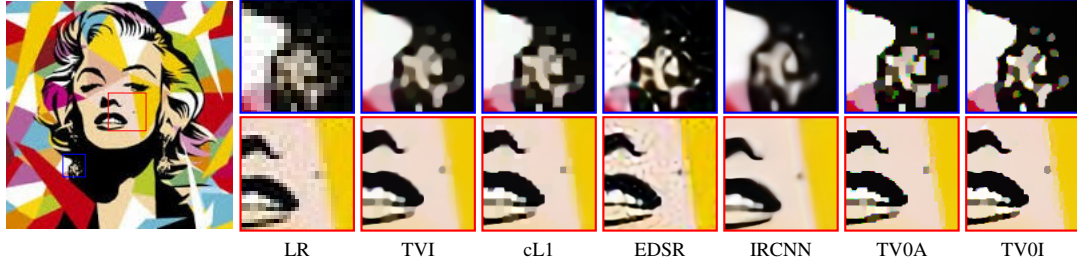


Figure 5: JPEG artefact removal by means of different SR models. For TVI, cL1, TV0A and TV0I the regularisation parameters are chosen as μ : 0.08, 0.05, 0.02, 0.02, respectively.

more cartoonized than the ones obtained by the other models. In particular TV and cL1 suffer from loss of contrast making small details hardly discernible while both IRCNN and EDSR produce a reconstruction with several artefacts due what has been discussed in Section V-B1.

3) Land-cover classification: The exploitation of Multi-Spectral Images (MSIs) is essential in the field of land-cover mapping and classification [33]. MSIs are satellite images whose numerous channels (from 4 to 200) are acquired at a different electromagnetic spectrum bandwidth, such as RGB or infrared bands, which quantifies different types of information about the objects in the recorded scene, such as their physical composition and their temperature to name a few. Existing segmentation techniques exploit these properties to label each pixel of the MSI with a class, thus producing a final 2D labelled image. These maps are essential in many sustainability-related applications and monitoring purposes for detecting land-cover changes (e.g. deforestation) over the years at the same geographical location, which cannot be done directly by simply looking at the MSIs (see [8], [34], [35] and references therein). Among the many existing open-source MSI datasets, we mention here e.g. the National Agriculture Imagery Program (NAIP) [36] dataset and the Hamlin Beach State Park (HBSP) [37] dataset. The former is a collection of multi-spectral aerial images (i.e. 1 meter resolution with three RGB channels), while the latter is a database multi-spectral images with 6 channels, 3 for the RGB and 3 for the infrared bands. This is indeed a benchmark dataset for validating the performance of deep-learning-based segmentation algorithms aiming to differentiate land objects with analogous characteristics (e.g. a grass from a tree), see [37]. For this problem, we apply the proposed jump-sparse SR method to increase the spatial resolution of the given MSI image and to output a pre-segmented image at the same time. The need of a SR model in this specific application is justified by the physical limitations preventing HR acquisitions, such as the limited spatial resolution in some bandwidths, such as the infrared band [38]. On the other hand, a simplified image where noise and blur artefacts have been removed is very handy for classification purposes. To compute the land-cover mapping on the output of the SR inverse Potts model we use in the following a standard k -Means segmentation and the state-of-the-art U-Net neural network [3] developed for segmentation tasks.

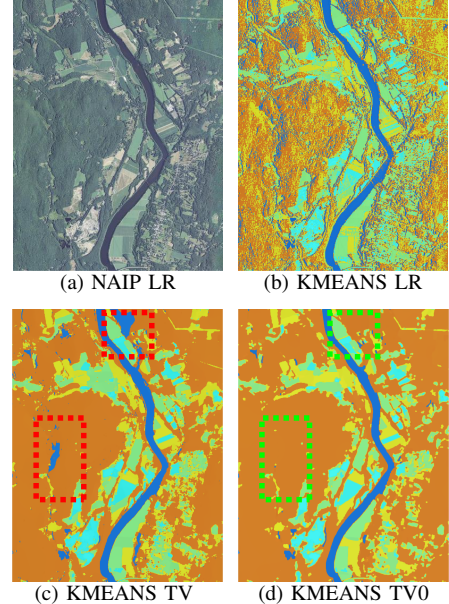


Figure 6: k -means segmentation with $k = 5$. In (c)-(d) the red and green boxes show possible misclassified details. (a) Given LR image (b) k -means classification of LR image (c) k -means classification of TV output (d) k -means classification of TV0I output.

In the first experiment we consider a LR test image ³ from the NAIP dataset (Figure 6 (a)). We start running the k -Means algorithm directly on this image, choosing empirically the number of classes to be $k = 5$. The classification obtained looks speckled and significant classification errors occur (see 6 (b)). In Figures 6 (c)-(d), we report the classification results obtained by applying k -Means to the TV and TV0I SR reconstructions (with $L = 2$). The segmentation results obtained on this gradient-sparsified image appear clearly much more reliable. We notice, in particular, that some parts of the vegetation are wrongly labelled as water in the TV result (red boxes), whereas this is not the case for the TV0I reconstruction (green boxes), due to its enhanced flattening properties.

In the second experiment we use the isotropic inverse Potts model for SR to pre-process an image from the validation set of the HBSP dataset before giving it as an input to the U-Net [37]. To do so, we consider a LR MSI acquisition of size $440 \times 350 \times 6$ and apply the model to each channel after

³Image identification number: M 4207221 NW 18 1 20120709

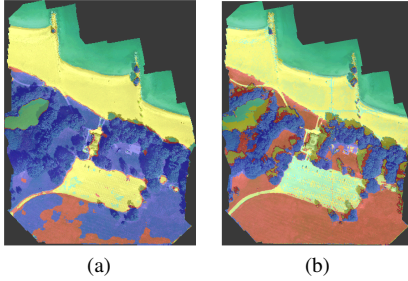


Figure 7: Results of multi-spectral image segmentation by means U-Net. (a) U-NET segmentation obtained starting from the given LR image. (b) U-NET segmentation obtained from the TVOI reconstruction.

setting $L = 2$. For comparisons, we use the U-Net on the given LR MSI and on the computed reconstruction. We report the results in Figure 7. Note, that differently from k -Means, U-NET does not require the user to specify the number of required classes. We observe that the quality of the U-Net segmentation is significantly improved by the SR TVOI pre-processing step. When applied to the given LR image (see Figure 7 (a)), the U-Net is in fact not capable to differentiate the group of trees (blue) from the grass (red). By increasing the resolution and promoting sparsity on the image gradient, seems to be of great help for achieving more accurate results.

VI. CONCLUSIONS

We considered the isotropic and anisotropic variants of the inverse Potts model focusing in particular on its use for super-resolution of images corrupted by blur and Gaussian noise. The use of non-convex jump-sparse regularisation has been originally proposed in [1] in the context of general 1D inverse problems and subsequently applied in [2], [14] to image segmentation and reconstruction problems, with only little focus on super-resolution problems. To overcome the computational limitations required by the use of the ADMM splitting considered in [1], [2], [14], we propose a novel ADMM algorithm allowing for the efficient solution of its subproblems by means of either hard-thresholding or standard CG solvers. For the proposed scheme we prove convergence results assuming specific growth conditions on the sequence of penalty parameters. We validate our model on synthetic images and test it on real-world examples where gradient-sparse super-resolution is required in view of an accurate recognition/classification step (QR code recognition [6], JPEG artefact removal and land-cover classification [33]). By numerous comparisons with convex and non-convex variational approaches, and with state-of-the-art deep learning methods [18], [21], we show that the proposed approach significantly improves classification precision, while limiting at the same times smoothing and loss-of-contrast artefacts in comparison with classical regularisations.

Further work should address the extension of the proposed convergence results to other gradient discretisations and less restrictive growth conditions for the sequence penalty parameters which were shown empirically to exhibit similar converging behaviours.

APPENDIX A CONVERGENCE ANALYSIS

We report here the convergence proofs of Theorem 2 and Theorem 3. We provide a detailed proof for Theorem 2 while providing only few details for Theorem 3 whose proof is based on essentially the same arguments.

A. Proof of Theorem 2

We consider the ADMM sequences (\mathbf{u}^k) , (\mathbf{t}^k) , (\mathbf{s}^k) , defined in (7)-(9). We want to show that there exists \mathbf{u}^* such that:

$$\mathbf{u}^k \rightarrow \mathbf{u}^*, \quad \mathbf{t}^k \rightarrow \mathbf{D}_h \mathbf{u}^*, \quad \mathbf{s}^k \rightarrow \mathbf{D}_v \mathbf{u}^*$$

We start defining the following functionals:

$$G_k^h(\mathbf{t}) := \mu \|\mathbf{t}\|_0 + \frac{\beta_t^k}{2} \|\mathbf{t} - (\mathbf{D}_h \mathbf{u}^k + \frac{\lambda_t^k}{\beta_t^k})\|_2^2,$$

$$G_k^v(\mathbf{s}) := \mu \|\mathbf{s}\|_0 + \frac{\beta_s^k}{2} \|\mathbf{s} - (\mathbf{D}_v \mathbf{u}^k + \frac{\lambda_s^k}{\beta_s^k})\|_2^2,$$

$$\begin{aligned} F_k(\mathbf{u}) := & \frac{1}{2} \|\mathbf{SHu} - \mathbf{g}\|_2^2 + \frac{\beta_t^k}{2} \|\mathbf{D}_h \mathbf{u} - (\mathbf{t}^{k+1} - \frac{\lambda_t^k}{\beta_t^k})\|_2^2 + \\ & + \frac{\beta_s^k}{2} \|\mathbf{D}_v \mathbf{u} - (\mathbf{s}^{k+1} - \frac{\lambda_s^k}{\beta_s^k})\|_2^2. \end{aligned}$$

Step 1: There holds:

$$\|\mathbf{t}^{k+1} - \mathbf{D}_h \mathbf{u}^k - \frac{\lambda_t^k}{\beta_t^k}\|_2^2 \leq \frac{2\mu N}{\beta_t^k}, \quad (18)$$

$$\|\mathbf{s}^{k+1} - \mathbf{D}_v \mathbf{u}^k - \frac{\lambda_s^k}{\beta_s^k}\|_2^2 \leq \frac{2\mu N}{\beta_s^k}. \quad (19)$$

These inequalities can trivially be shown by the minimality of \mathbf{t}^{k+1} and \mathbf{s}^{k+1} which entail in particular $G_k^h(\mathbf{t}^{k+1}) \leq G_k^h(\mathbf{D}_h \mathbf{u}^k + \frac{\lambda_t^k}{\beta_t^k})$ and $G_k^v(\mathbf{s}^{k+1}) \leq G_k^v(\mathbf{D}_v \mathbf{u}^k + \frac{\lambda_s^k}{\beta_s^k})$. From the first inequality we get:

$$\begin{aligned} & \mu \|\mathbf{t}^{k+1}\|_0 + \frac{\beta_t^k}{2} \|\mathbf{t}^{k+1} - (\mathbf{D}_h \mathbf{u}^k + \frac{\lambda_t^k}{\beta_t^k})\|_2^2 \\ & \leq \mu \|\mathbf{D}_h \mathbf{u}^k + \frac{\lambda_t^k}{\beta_t^k}\|_0 \leq 2N, \end{aligned}$$

by definition of $\|\cdot\|_0$. By neglecting the first term on the LHS of the inequality above we deduce (18). The bound (19) can be deduced similarly. From (18) and (19) and since $(\beta_t^k) \nearrow +\infty$ we have:

$$\|\mathbf{t}^{k+1} - \mathbf{D}_h \mathbf{u}^k - \frac{\lambda_t^k}{\beta_t^k}\|_2^2 \rightarrow 0, \quad \|\mathbf{s}^{k+1} - \mathbf{D}_v \mathbf{u}^k - \frac{\lambda_s^k}{\beta_s^k}\|_2^2 \rightarrow 0 \quad (20)$$

Step 2: By minimality of \mathbf{u}^{k+1} we have: $F_k(\mathbf{u}^{k+1}) \leq F_k(\mathbf{u}^k)$ for every k . By definition of F_k and applying (18)-(19), we deduce:

$$\begin{aligned} & \frac{1}{2} \|\mathbf{SHu}^{k+1} - \mathbf{g}\|_2^2 + \frac{\beta_t^k}{2} \|\mathbf{D}_h \mathbf{u}^{k+1} - \mathbf{t}^{k+1} + \frac{\lambda_t^k}{\beta_t^k}\|_2^2 + \\ & + \frac{\beta_s^k}{2} \|\mathbf{D}_v \mathbf{u}^{k+1} - \mathbf{s}^{k+1} + \frac{\lambda_s^k}{\beta_s^k}\|_2^2 \leq \end{aligned} \quad (21)$$

$$\begin{aligned} & \frac{1}{2} \|\mathbf{SHu}^k - \mathbf{g}\|_2^2 + \frac{\beta_t^k}{2} \|\mathbf{D}_h \mathbf{u}^k - \mathbf{t}^{k+1} + \frac{\lambda_t^k}{\beta_t^k}\|_2^2 + \\ & + \frac{\beta_s^k}{2} \|\mathbf{D}_v \mathbf{u}^k - \mathbf{s}^{k+1} + \frac{\lambda_s^k}{\beta_s^k}\|_2^2 \leq \frac{1}{2} \|\mathbf{SHu}^k - \mathbf{g}\|_2^2 + 2\mu N. \end{aligned}$$

Now, by neglecting independently the second and third term on the LHS we deduce:

$$\frac{1}{2}\|\mathbf{SHu}^{k+1} - \mathbf{g}\|_2^2 \leq \frac{1}{2}\|\mathbf{SHu}^k - \mathbf{g}\|_2^2 + 2\mu N,$$

which can be recursively iterated, thus getting the following relation which holds for every $k \geq 1$:

$$\frac{1}{2}\|\mathbf{SHu}^k - \mathbf{g}\|_2^2 \leq \frac{1}{2}\|\mathbf{SHu}^0 - \mathbf{g}\|_2^2 + 2\mu Nk.$$

By now neglecting the first and the third non-negative term on the LHS of (21) and using the estimate above, we can deduce the following:

$$\begin{aligned} \frac{\beta_t^k}{2}\|\mathbf{D}_h\mathbf{u}^{k+1} - \mathbf{t}^{k+1} + \frac{\boldsymbol{\lambda}_t^k}{\beta_t^k}\|_2^2 \leq \\ \frac{1}{2}\|\mathbf{SHu}^k - \mathbf{g}\|_2^2 + 2\mu N \leq \frac{1}{2}\|\mathbf{SHu}^0 - \mathbf{g}\|_2^2 + 2\mu Nk, \end{aligned}$$

which entails:

$$\|\mathbf{D}_h\mathbf{u}^{k+1} - \mathbf{t}^{k+1} + \frac{\boldsymbol{\lambda}_t^k}{\beta_t^k}\|_2^2 \leq \frac{1}{\beta_t^k}\|\mathbf{SHu}^0 - \mathbf{g}\|_2^2 + 4\mu N \frac{k}{\beta_t^k}.$$

By assumption $(\beta_t^k) \nearrow +\infty$ and $\frac{k}{\beta_t^k} \rightarrow 0$, which, combined with the boundedness of the quadratic term entails:

$$\|\mathbf{D}_h\mathbf{u}^{k+1} - \mathbf{t}^{k+1} + \frac{\boldsymbol{\lambda}_t^k}{\beta_t^k}\|_2^2 \rightarrow 0, \quad (22)$$

and, similarly, that:

$$\|\mathbf{D}_v\mathbf{u}^{k+1} - \mathbf{s}^{k+1} + \frac{\boldsymbol{\lambda}_s^k}{\beta_s^k}\|_2^2 \rightarrow 0.$$

Step 3: We show that the sequences $\mathbf{D}_h\mathbf{u}^k$ and $\mathbf{D}_v\mathbf{u}^k$ are Cauchy sequences, hence they converge. We prove this for $\mathbf{D}_h\mathbf{u}^k$, the proof for $\mathbf{D}_v\mathbf{u}^k$ is identical.

$$\begin{aligned} \|\mathbf{D}_h\mathbf{u}^{k+1} - \mathbf{D}_h\mathbf{u}^k\|_2 &\leq \\ &\leq \|\mathbf{D}_h\mathbf{u}^{k+1} - \mathbf{t}^{k+1} + \frac{\boldsymbol{\lambda}_t^k}{\beta_t^k}\|_2 + \|\mathbf{D}_h\mathbf{u}^k - \mathbf{t}^{k+1} + \frac{\boldsymbol{\lambda}_t^k}{\beta_t^k}\|_2. \end{aligned}$$

From (20) and (22) the RHS tends to 0 as $k \rightarrow +\infty$. As a consequence, $\mathbf{D}_h\mathbf{u}^k$ is a Cauchy sequence, which thus converges to a point \mathbf{t}^* . Similarly, $\mathbf{D}_v\mathbf{s}^k$ which converges to some \mathbf{s}^* .

Step 4: We start rewriting (10):

$$\frac{\boldsymbol{\lambda}_t^{k+1}}{\beta_t^k} = \mathbf{D}_h\mathbf{u}^{k+1} - \mathbf{t}^{k+1} + \frac{\boldsymbol{\lambda}_t^k}{\beta_t^k}. \quad (23)$$

By (22), the RHS of this equation tends to 0 as $k \rightarrow \infty$, whence we deduce that $\frac{\|\boldsymbol{\lambda}_t^{k+1}\|_2}{\sqrt{\beta_t^k}} \rightarrow 0$. By monotonicity of the (β_t^k) we then deduce that $\frac{\|\boldsymbol{\lambda}_t^k\|_2}{\sqrt{\beta_t^k}} \rightarrow 0$. By (23), and proceeding similarly for the sequences (\mathbf{s}^k) and $(\mathbf{D}_v\mathbf{u}^k)$, we deduce the following:

$$\begin{aligned} \|\mathbf{D}_h\mathbf{u}^{k+1} - \mathbf{t}^{k+1}\|_2 &\leq \frac{\|\boldsymbol{\lambda}_t^{k+1}\|_2 + \|\boldsymbol{\lambda}_t^k\|_2}{\sqrt{\beta_t^k}}, \\ \|\mathbf{D}_v\mathbf{u}^{k+1} - \mathbf{s}^{k+1}\|_2 &\leq \frac{\|\boldsymbol{\lambda}_s^{k+1}\|_2 + \|\boldsymbol{\lambda}_s^k\|_2}{\sqrt{\beta_s^k}}, \end{aligned}$$

where both quantities on the RHS tend to 0 as $k \rightarrow \infty$. Therefore, \mathbf{t}^k converges to \mathbf{t}^* as well as $\mathbf{D}_h\mathbf{u}^k$ and \mathbf{s}^k converges to \mathbf{s}^* as well as $\mathbf{D}_v\mathbf{u}^k$, by uniqueness of the limit.

Step 5: We can now prove the convergence of \mathbf{u}^k . For simplicity, let us define the quantities $\mathbf{A} := \mathbf{SH}$ and $\mathbf{M}_k := \frac{1}{\beta_t^k}\mathbf{A}^T\mathbf{A} + \mathbf{D}_h^T\mathbf{D}_h + \frac{\beta_s^k}{\beta_t^k}\mathbf{D}_v^T\mathbf{D}_v$, for every k . Since the operators \mathbf{D}_h and \mathbf{D}_v are both full rank, we observe that the matrix \mathbf{M}_k is invertible and symmetric for all k . The optimality condition of problem (9) reads:

$$\mathbf{M}_k\mathbf{u}^k = \mathbf{D}_h^T(\mathbf{t}^{k+1} - \frac{\boldsymbol{\lambda}_t^k}{\beta_t^k}) + \frac{\beta_s^k}{\beta_t^k}\mathbf{D}_v^T(\mathbf{s}^{k+1} - \frac{\boldsymbol{\lambda}_s^k}{\beta_t^k}) + \frac{1}{\beta_t^k}\mathbf{A}^T\mathbf{g}.$$

Since $\mathbf{t}^{k+1} \rightarrow \mathbf{t}^*$, $\mathbf{s}^{k+1} \rightarrow \mathbf{s}^*$, $\frac{\boldsymbol{\lambda}_t^k}{\beta_t^k} \rightarrow 0$, $\frac{\boldsymbol{\lambda}_s^k}{\beta_t^k} \rightarrow 0$ by the previous steps, \mathbf{D}_h^T and \mathbf{D}_v^T are continuous operators since they are bounded, $\frac{\beta_s^k}{\beta_t^k} \rightarrow c$ by hypothesis, and $\frac{1}{\beta_t^k}\mathbf{A}^T\mathbf{g} \rightarrow 0$ by the assumption $(\beta_t^k) \nearrow +\infty$, the RHS converges pointwise to $\mathbf{z}^* = \mathbf{D}_h^T\mathbf{t}^* + c\mathbf{D}_v^T\mathbf{s}^*$. Therefore, $\mathbf{M}_k\mathbf{u}^k \rightarrow \mathbf{z}^*$. Additionally, the sequence \mathbf{M}_k^{-1} converges pointwise to a continuous operator \mathbf{M}^* . We thus have that $\mathbf{M}_k^{-1}\mathbf{M}_k\mathbf{u}^k \rightarrow \mathbf{M}^*\mathbf{z}^*$, or equivalently, $\mathbf{u}^k \rightarrow \mathbf{M}^*\mathbf{z}^* := \mathbf{u}^*$. We now want to show that $\mathbf{t}^* = \mathbf{D}_h\mathbf{u}^*$ and, similarly, that $\mathbf{s}^* = \mathbf{D}_v\mathbf{u}^*$. We show the details only for the former case. By the triangle inequality we get:

$$\begin{aligned} \|\mathbf{t}^* - \mathbf{D}_h\mathbf{u}^*\|_2 &\leq \|\mathbf{t}^* - \mathbf{D}_h\mathbf{u}^k\|_2 + \|\mathbf{D}_h\mathbf{u}^k - \mathbf{D}_h\mathbf{u}^*\|_2 \\ &\leq \|\mathbf{t}^* - \mathbf{D}_h\mathbf{u}^k\|_2 + \|\mathbf{D}_h\mathbf{u}^k\| \|\mathbf{u}^k - \mathbf{u}^*\|_2, \end{aligned}$$

where the both terms tend to 0 by what shown in Step 3 and above. This concludes the proof.

B. Proof of Theorem (3)

The proof of Theorem (3) follows the same steps as the previous one. The only main difference in it is the definition of \mathbf{M}_k , which reads in this case:

$$\mathbf{M}_k := \frac{1}{\beta^k}\mathbf{A}^T\mathbf{A} + \mathbf{D}^T\mathbf{D} = \frac{1}{\beta^k}\mathbf{A}^T\mathbf{A} + \mathbf{D}_h^T\mathbf{D}_h + \mathbf{D}_v^T\mathbf{D}_v.$$

By proceeding similarly as above the conclusion holds.

ACKNOWLEDGMENTS

LC and PC acknowledge the support received by the Academy "Complex Systems" of the JEDI IDEX of the Université Côte d'Azur.

REFERENCES

- [1] M. Storath, A. Weinmann, and L. Demaret, "Jump-sparse and sparse recovery using Potts functionals," *IEEE Trans. Signal Process.*, vol. 62, no. 14, pp. 3654–3666, 2014.
- [2] M. Storath, A. Weinmann, J. Frikel, and M. Unser, "Joint image reconstruction and segmentation using the Potts model," *Inverse Probl.*, vol. 31, no. 2, pp. 025003, 29, 2015.
- [3] O. Ronneberger, P. Fischer, and T. Brox, "U-net: Convolutional networks for biomedical image segmentation," in *MICCAI 2015*. Cham: Springer International Publishing, 2015, pp. 234–241.
- [4] C. G. Galbraith and J. A. Galbraith, "Super-resolution microscopy at a glance," *Journal of Cell Science*, vol. 124, no. 10, pp. 1607–1611, 2011.
- [5] R. M. Willett, I. Jermyn, R. D. Nowak, and J. Zerubia, "Wavelet-Based Superresolution in Astronomy," in *ADASS XIII*, vol. 314, 2004, p. 107.
- [6] Y. Kato, D. Deguchi, T. Takahashi, I. Ide, and H. Murase, "Low resolution QR-code recognition by applying super-resolution using the property of qr-codes," in *ICDAR 2011*, vol. IEEE ICDAR, pp. 992–996.
- [7] F. Ling, Y. Zhang, G. M. Foody, X. Li, X. Zhang, S. Fang, W. Li, and Y. Du, "Learning-based superresolution land cover mapping," *IEEE Trans. Geosci. Remote Sens.*, vol. 54, no. 7, pp. 3794–3810, 2016.

[8] J. Wickham, C. Homer, J. Vogelmann, A. McKerrow, R. Mueller, N. Herold, and J. Coulston, "The multi-resolution land characteristics (MRLC) consortium—20 years of development and integration of USA national land cover data," *Remote Sens.*, vol. 6, pp. 7424–7441, 2014.

[9] S. Chaudhuri, *Super-Resolution Imaging*. Springer US, 2001, vol. International Series in Engineering and Computer Science, no. 632.

[10] L. Yue, H. Shen, J. Li, Q. Yuan, H. Zhang, and L. Zhang, "Image super-resolution: The techniques, applications, and future," *Signal Process.*, vol. 128, 2016.

[11] T. F. Chan, M. K. Ng, A. C. Yau, and A. M. Yip, "Superresolution image reconstruction using fast inpainting algorithms," *Appl. Comput. Harmon. A.*, vol. 23, no. 1, pp. 3–24, 2007.

[12] S. J. O. A. Marquina, "Image super-resolution by TV-regularization and bregman iteration," *J. Sci. Comput.*, vol. 37, pp. 367–382, 2008.

[13] W. Yao, J. Shen, Z. Guo, J. Sun, and B. Wu, "A total fractional-order variation model for image super-resolution and its SAV algorithm," *J. Sci. Comput.*, vol. 82, no. 3, pp. 1–18, 2020.

[14] M. Storath, D. Rickert, M. Unser, and A. Weinmann, "Fast segmentation from blurred data in 3D fluorescence microscopy," *IEEE Trans. Image Process.*, vol. 26, no. 10, pp. 4856–4870, 2017.

[15] L. Xu, C. Lu, Y. Xu, and J. Jia, "Image smoothing via l_0 gradient minimization," *ACM Trans. Graph (SIGGRAPH Asia)*, 2011.

[16] W. Yang, X. Zhang, Y. Tian, W. Wang, J.-H. Xue, and Q. Liao, "Deep learning for single image super-resolution: A brief review," *IEEE Transactions on Multimedia*, vol. 21, no. 12, pp. 3106–3121, 2019.

[17] Z. Wang, J. Chen, and S. C. Hoi, "Deep learning for image super-resolution: A survey," *IEEE Trans. Pattern Anal. Mach. Intell.*, 2020.

[18] B. Lim, S. Son, H. Kim, S. Nah, and K. Mu Lee, "Enhanced deep residual networks for single image super-resolution," in *Proceedings of the IEEE CVPR*, 2017, pp. 136–144.

[19] S. V. Venkatakrishnan, C. A. Bouman, and B. Wohlberg, "Plug-and-play priors for model based reconstruction," in *IEEE GlobalSIP 2013*, pp. 945–948.

[20] S. H. Chan, X. Wang, and O. A. Elgendi, "Plug-and-play ADMM for image restoration: Fixed-point convergence and applications," *IEEE Trans. Comp. Imag.*, vol. 3, no. 1, pp. 84–98, 2016.

[21] K. Zhang, W. Zuo, S. Gu, and L. Zhang, "Learning deep CNN denoiser prior for image restoration," in *Proceedings of the IEEE CVPR*, 2017, pp. 3929–3938.

[22] Y. Boykov, O. Veksler, and R. Zabih, "Fast approximate energy minimization via graph cuts," *IEEE Trans. Pattern Anal. Mach. Intell.*, vol. 23, no. 11, pp. 1222–1239, 2001.

[23] Y. Wang, J. Yang, W. Yin, and Y. Zhang, "A new alternating minimization algorithm for total variation image reconstruction," *SIIMS*, vol. 1, no. 3, pp. 248–272, 2008.

[24] C. Wu and X.-C. Tai, "Augmented lagrangian method, dual methods, and split bregman iteration for ROF, vectorial TV, and high order models," *SIIMS*, vol. 3, no. 3, pp. 300–339, 2010.

[25] T. Blumensath and M. E. Davies, "Iterative hard thresholding for compressed sensing," *Appl. Comput. Harmon. A.*, vol. 27, no. 3, pp. 265–274, 2009.

[26] Y. Boykov and V. Kolmogorov, "An experimental comparison of min-cut/max-flow algorithms for energy minimization in vision," *IEEE Trans. Pattern Anal. Mach. Intell.*, vol. 26, no. 9, pp. 1124–1137, 2004.

[27] C. E. Duchon, "Lanczos filtering in one and two dimensions," *J. Appl. Meteorol.*, vol. 18, no. 8, pp. 1016–1022, 1979.

[28] T. Zhang, "Multi-stage convex relaxation for learning with sparse regularization," in *Adv. Neural. Inf. Process. Syst.*, 2009, pp. 1929–1936.

[29] E. Agustsson and R. Timofte, "NTIRE 2017 challenge on single image super-resolution: Dataset and study," in *Proceedings of the IEEE CVPR*, 2017, pp. 126–135.

[30] Zhou Wang, A. C. Bovik, H. R. Sheikh, and E. P. Simoncelli, "Image quality assessment: from error visibility to structural similarity," *IEEE Trans. Image Process.*, vol. 13, no. 4, pp. 600–612, 2004.

[31] D. Sage, T.-A. Pham, H. Babcock, T. Lukes, T. Pengo, J. Chao, R. Velmurugan, A. Herbert, A. Agrawal, S. Colabrese, A. Wheeler, A. Archetti, B. Rieger, R. Ober, G. M. Hagen, J.-B. Sibarita, J. Ries, R. Henriques, M. Unser, and S. Holden, "Super-resolution fight club: assessment of 2D and 3D single-molecule localization microscopy software," *Nature methods*, vol. 16, no. 5, p. 387–395, May 2019.

[32] S. Ono, " l_0 gradient projection," *IEEE Trans. Image Process.*, vol. 26, no. 4, pp. 1554–1564, 2017.

[33] J. Cihlar, "Land cover mapping of large areas from satellites: status and research priorities," *Int. J. Remote Sens.*, vol. 21, no. 6–7, pp. 1093–1114, 2000.

[34] K. Malkin, C. Robinson, L. Hou, R. Soobitsky, J. Czawlytko, D. Samaras, J. Saltz, L. Joppa, and N. Jojic, "Label super-resolution networks," in *ICLR*, 2018.

[35] F. Franci, E. Mandanici, and G. Bitelli, "Remote sensing analysis for flood risk management in urban sprawl contexts," *Geomatics, Nat. Hazards Risk*, vol. 6, no. 5–7, pp. 583–599, 2015.

[36] A. E. Maxwell, T. A. Warner, B. C. Vanderbilt, and C. A. Ramezan, "Land cover classification and feature extraction from national agriculture imagery program (NAIP) orthoimagery: A review," *ISPRS*, vol. 83, no. 11, pp. 737–747, 2017.

[37] R. Kemker, C. Salvaggio, and C. Kanan, "High-resolution multispectral dataset for semantic segmentation," *arXiv preprint arXiv:1703.01918*, 2017.

[38] P. Cascarano, F. Corsini, S. Gandolfi, E. L. Piccolomini, E. Mandanici, L. Tavasci, and F. Zama, "Super-resolution of thermal images using an automatic total variation based method," *Remote Sens.*, vol. 12, no. 10, p. 1642, 2020.

Pasquale Cascarano received his master degree in Mathematics in 2018 at University of Bologna. He is currently a Ph.D. student in Applied Mathematics at the University of Bologna (IT). His research focuses on variational and deep learning methods for imaging inverse problems.



Luca Calatroni completed his Ph.D. in Applied Mathematics in 2015 as part of the Cambridge Image Analysis research group (UK). He was then a Marie Skłodowska-Curie research fellow at the University of Genova (Italy) and *Lecteur Hadamard* FMJH fellow at the École Polytechnique (France). From October 2019, he is permanent CNRS researcher at the I3S laboratory in Sophia Antipolis (France) within the Morpheme research group. His research focuses on variational methods and non-smooth optimisation algorithms for imaging and vision.



Elena Loli Piccolomini is Professor of Numerical Analysis at the University of Bologna. Her research topics are regularisation methods for inverse problems in imaging, with particular focus on medical imaging and tomographic image reconstruction.

